# Active noise control with resonant flush-mounted piezoelectric cells in the presence of airflow: Wind tunnel experiments

Jonathan Rodriguez, Mouhamed Ezzine, Manuel Collet, Vincent Clair

# Active Noise Control for Stator Vanes using Resonant Flush-Mounted Piezoelectric Cells : Wind Tunnel Experiments

Jonathan Rodriguez

*Univ Lyon, INSA Lyon, CNRS, LaMCoS, UMR5259, 69621 Villeurbanne, France. Author email: jonathan.rodriguez@insa-lyon.fr*

Mouhamed Ezzine and Manuel Collet

*Université de Lyon, Ecole Centrale de Lyon, LTDS UMR CNRS 5513, F-69134 Ecully, France.*

Vincent Clair

*Université de Lyon, Ecole Centrale de Lyon, LMFA UMR CNRS 5509, F-69134 Ecully, France*

**Abstract**

Methods and technologies to control the noise coming from turbulent flows impinging on outlet guide vanes in turbofan engines are tremendously needed nowadays to comply with new legislation on acoustic environment pollution. The following manuscript relies on preliminary research proposing a new experimental design of active noise control system to be integrated into a jet engine outer guide vane prototype, consisting of multiple flush-mounted piezoelectric cells. Hence, three active cells are placed into a wind tunnel with upstream acoustic excitation generating grazing incident waves and different airflow velocities. Using a downstream microphone as an error sensor, the active system succeeds in improving the transmission loss of the sample by 2.5dB at the target frequency (670Hz) corresponding to the main piezoacoustic mode with airflow velocities up to 20m.s$^{-1}$. Even small, these early experimental results confirm the ability of the concept to interact with the ambient acoustics without disturbing the airflow as in passive solutions using porous materials for instance, leading the path to future experiments with realistic turbulence generating acoustic sources on the leading edge of the vane profile.

*Keywords:* Active noise control, Outlet guide vane, Grazing incidence, Turbofan engine

## 1. Introduction

In the past years, international regulations have become more and more severe regarding environmental noise pollution. With the increase of air traffic around airports, aircraft noise pollution has logically become a major concern, and methods and technologies to address this problem are concentrating a lot of effort from manufacturers and researchers. Thus, the main objective of these new noise control systems is to reduce the noise emitted by turbofan engines [1] due to airflow-airfoil interactions inside the jet engine nacelle.

One of the main noise sources comes from the fluid/structure interaction between vortices created by the rotor blades passing and the leading edge of the stator vanes or outlet guide vanes (OGV) located downstream. To achieve significant noise attenuation at the stator level, 3 methods are available [2, 3, 4, 5]: geometry optimization, passive control materials, and active control.

Applied to vanes profiles, geometry optimization solutions include swept and/or leaned stator [6] and serrations on the leading or trailing edge [7, 8]. In passive structural acoustic control, softer vanes or acoustic liners at the inlet of turbofan engines [9] can be used to add noise dissipation to the struc-

*Accepted Manuscript. Version of Record available at https://doi.org/10.1177/10775463231210031

ture. A very common solution is the use of porous materials [10] with cavities of different size acting as Helmholtz resonators that can provide excellent noise attenuation for both tonal and broadband disturbance. Although widely used, these materials often represent a non-negligible additional weight and volume inside the structure. Moreover, such modifications of airfoil geometry or boundary layer can also result in noise amplification at particular conditions and degradation of aerodynamic performance which is the most severe consequence.

Thus, active stator vanes can be considered relevant technological solutions for their lightweight and closeness to the noise source, providing the theoretical opportunity to reduce by 80% the downstream radiated noise [11]. However, two major difficulties arise from the location of the actuators: many of the acoustic control problems, especially when optimizing the transmission loss are addressed with normal wave incidence, giving maximum control authority to actuators oriented directly toward the acoustic wave velocity vector [12, 13].

In addition, for experiments within ducts including or not airflow, the control actuators are in general loudspeakers [14], which facilitate the control of the acoustic field for obvious physical reasons. Nevertheless, these actuators are heavy and require a certain available volume to be implemented. This last constraint is not consistent with the considered thin OGV profiles inside the turbofan engine.

Early attempts have been made to implement piezoelectric transducers at the surface of OGVs with the objective of acoustic control. For instance, Curtis, A. R. in 1999 [15] used flush mounted PZT5A transducers on stator vanes. A 3 to 6dB attenuation for tonal excitation was achieved with transducers supplied by 150V. Besides, the authors pointed out the difficulty to obtain sufficient acoustic controllability with this type of thin actuator.

Galland et al. [16] and Sellen et al. [17] developed hybrid actuators with a piezoelectric transducer driving a membrane inside a small cavity. Combining the high-frequency performance of the passive part and the low-frequency performance of the active one, up to 20dB gain on the transmission loss (TL) was achieved within a duct with different airflow velocities. Still, the volume necessary for the actuator, its membrane flexibility, and its wire mesh surface structure are not compatible with our specific need for a flush-mounted control system for a thin OGV profile to not disturb the flow and maintain static pressure.

Hence, the following manuscript proposes preliminary experimental results on a new proposition of an active noise control system dedicated to reducing the acoustic emission from the interaction turbulence/airfoil on the leading edge of stator vanes. The concept consists of flush-mounted piezoelectric cells optimized in their design to take advantage of their main electromechanical resonance and control the noise within the desired bandwidth on a downstream target microphone.

The manuscript is organized as follows: Section 2 presents the prototype design with its electromechanical and electro-acoustical behavior. Then Section 3 details the experimental setup with the acoustic and airflow duct. The Section 4 develops the identification process and the active control design. Finally, Section 5 addresses the experimental results obtained in terms of transmission and insertion loss thanks to the active control system.

## 2. Active flush-mounted cells design

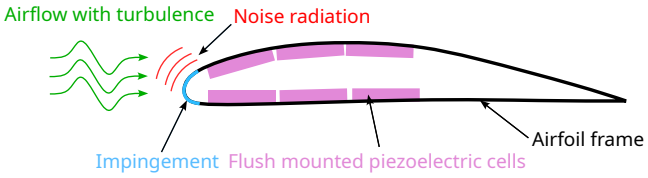


Figure 1: Active vibration and noise control system principle for aerodynamic profile.

The present section introduces the prototype mechanical design initiated in [18] and the electro-acoustical behavior of the cells within the experimental setup of the wind tunnel. As mentioned earlier, the proposed active noise control system is aimed to reduce the noise level emitted by the interaction between a turbulent airflow coming from the rotor vanes and the airfoil surface of the OGV as illustrated in Figure 1. Each one of the purple rectangles is a piezoelectric actuator whose functioning principle is depicted in the Figures 2 and 3. Thus, each piezoelectric cell is constituted by a thin 1mm aluminum skin of $44 \times 44$mm with 6 transducers fixed with epoxy resin and connected in parallel. The transducers, in green color, are PZT-5A piezoelectric stack of $10 \times 5$mm section and 2mm thickness in the strain direction ($d_{33}$). The mechanical mounting wedges have been optimized to improve

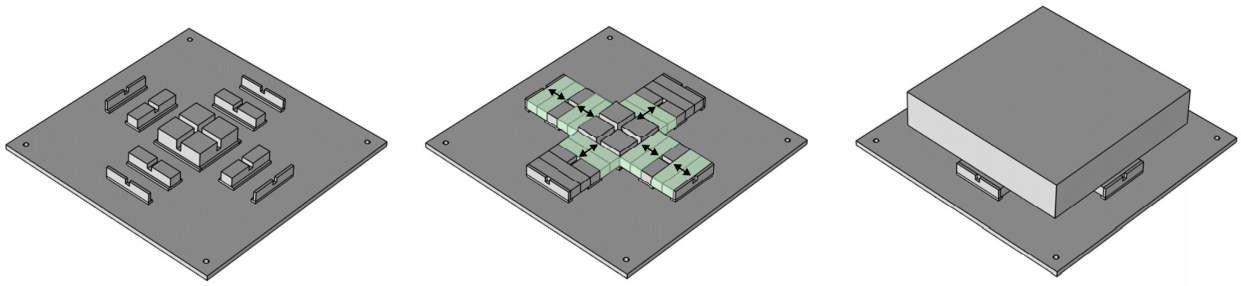

(a) (b) (c)

Figure 2: 3D representations of each piezoelectric cell architecture : (a) aluminum skin alone, (b) 6 operational transducers (green color) with their main strain direction under electric excitation, (c) additional mass.

the effective piezoacoustic coupling. The main idea is to design a high-frequency acoustic actuator by maximizing the moving surface of the cell for a certain bandwidth and also the electromechanical coupling. Since the aluminum skin remains rigid, additional steel masses of 168g have been added to guarantee sufficient electromechanical coupling within the desired bandwidth.

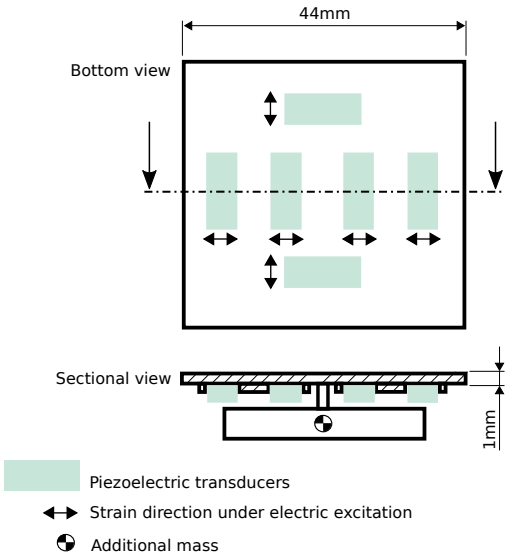


Figure 3: Schematic representation of the piezoelectric transducers implementation on each cell.

The manufactured prototype of the outer vane profile consists of 3 operational flush-mounted piezoelectric cells to be installed in a wind tunnel for preliminary experiments as displayed in Figure 4. Unfortunately, cells #4 and #5 presented electromechanical issues during the experiment due to the manufacturing process, and were disconnected to not disturb the dynamic behavior of the remaining operational cells #1 to #3.

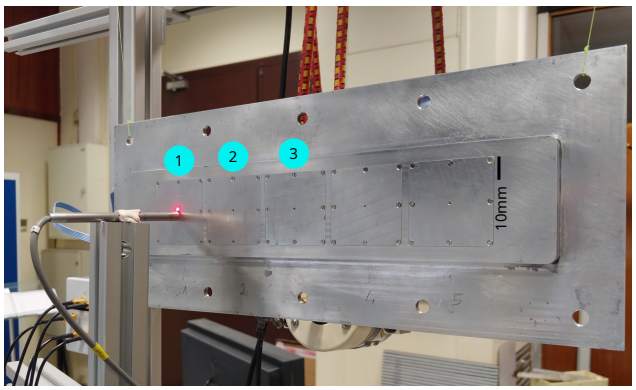


Figure 4: Active noise control system overview with operational cells #1 to #3 and scale

.

## 3. Experimental setup

The operational prototype cells are installed in a wind tunnel with a rectangular section of 68 × 110mm. Figure 5 provides a schematic representation of the experimental setup in addition with pictures in Figure 6. First, a constant airflow, controllable in velocity enters the tunnel through an inlet section and goes out through an anechoic outlet. At the upstream section and isolated from the airflow, a loudspeaker is used as an external acoustic source. The active cells are then positioned at the reference position $x = 0$ and 4 microphones

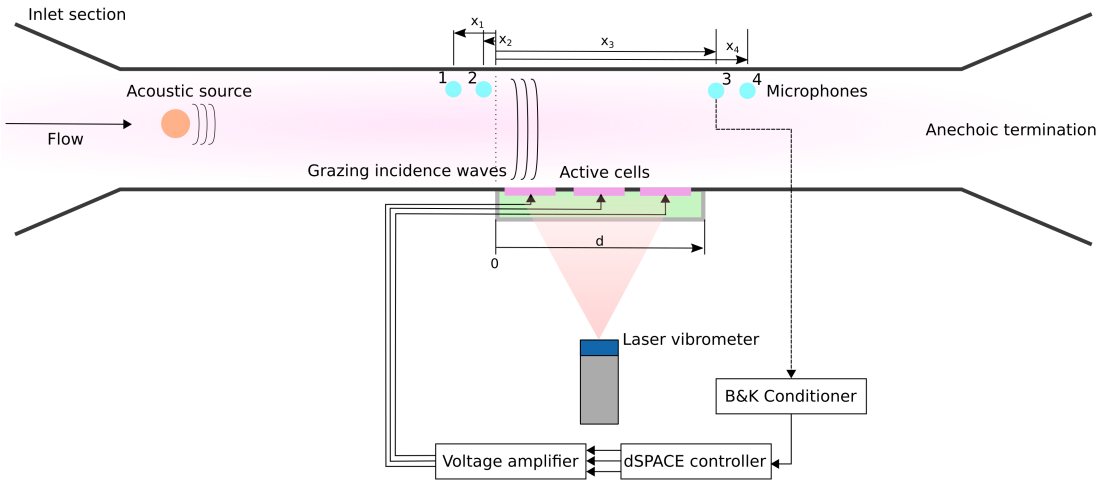


Figure 5: Wind tunnel experiment schematic representation.

measure the acoustic pressure at positions upstream ($x_1$ and $x_2$) and downstream ($x_3$ and $x_4$). The microphone positions are given in Table 1. Since the reference duct has almost no acoustic reflection, these 4 microphones are dedicated to estimating the transmission loss (TL) of the active prototype.

| Microphone | Position [mm] |
|---|---|
| $x_1$ | $-135$ |
| $x_2$ | $-100$ |
| $d$ | 453 |
| $x_3$ | 550 |
| $x_4$ | 585 |

Table 1: microphones positions inside the duct and active sample length.

Considering the active control part, the error microphone is selected to be the #3. Thus, it is connected to both the acquisition system and a dSPACE MicroLabBox controller. The controller then generates a voltage command signal of $+/-$ 10V for each active cell which is amplified by a $10\times$ gain through a voltage amplifier, leveling up the piezoelectric supply voltage to $+/-100$V. Finally, the following acoustic control experiment is realized using an airflow velocity inside the duct between 0 and 20m.s$^{-1}$ (Mach 0.06).

## 4. System identification and control

The following section describes the identification process of the piezoacoustic system between the cell voltage command signals and the error microphone response without airflow. Then, a modal-shaped LQG controller is derived to target the maximum acoustic controllability bandwidth of the control system.

### *4.1. Piezoacoustic system response*

First, the multi single-input/single-output (MSISO) control system considered is defined and a schematic representation is displayed on Figure 7. Hence, $y(t)$ is the microphone output signal (error signal). The transfer functions $H_{ij}(s)$ with $s = \mathbf{j}\omega$ as the Laplace variable, define the effect of actuator $i$ on sensor $j$ with $i \in \{1, 2, 3\}$ and $j \in \{1, 2\}$ (1 for microphone and 2 for the laser vibrometer). The controller transfer functions are then defined by $K_i(s)$ and their output control signal $u_i(t)$.

The frequency response functions (FRF) measurement of the error microphone responses to the excitation of the control system is realized by sending to each one of the active cells a band-limited white noise with a sampling frequency of 50kHz and maximum amplitude 10V. In addition, a Polytec PSV500 laser vibrometer measures from behind the cells the mechanical vibration of the active aluminum surfaces to observe the electromechanical coupling of the system and compare it to the piezoacoustic coupling characterizing its performance.

The measured FRFs $H_{i1}(f)$, $H_{i2}(f)$ and their spectral coherence are displayed on the Figures 8, 9 and 10 respectively. One can clearly notice that each cell has a different acoustic impact on the


(a)

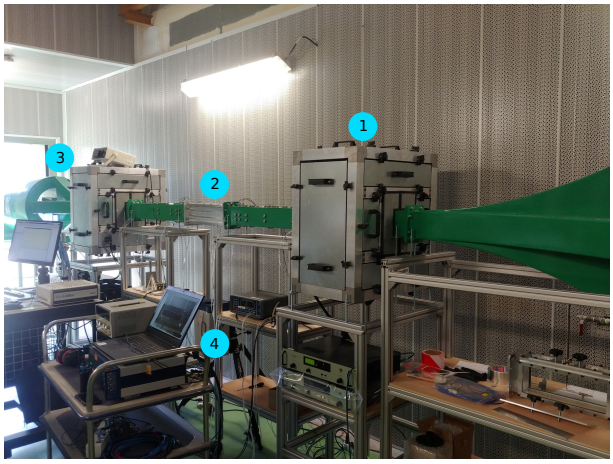


(b)

Figure 6: Wind tunnel experiment: (a) view from downstream (b) view from upstream, (1) acoustic source, (2) active sample, (3) anechoic outlet, (4) laser vibrometer.

environment in the frequency domain. Cell #1 presents a main electro-acoustic mode at $f_1 = 450$ $Hz$, cell #2 has the lowest coupling and acts at 470Hz and 610Hz. Finally, cell #3 shows the best piezoacoustic coupling at 670Hz. Besides, the measured FRFs $H_{i2}(f)$, when compared to their acoustic counterpart $H_{i1}(f)$ present higher amplitudes and better spectral coherence for a larger bandwidth. This major observation demonstrates that although the system is well designed with a good electro-mechanical coupling with this configuration of piezoelectric transducers, it still must be optimized further to generate more acoustic pressure on the aluminum skin surface to improve the piezoacoustic coupling. The observed discrepancies between all piezoelectric cells come from small differences occurring during wedges manufacturing and piezoelectric layer gluing. One can also underline the main importance of the membrane clamping that modifies the frequency of the main electromechanical mode. This sensitivity shall be considered in future optimization and design.

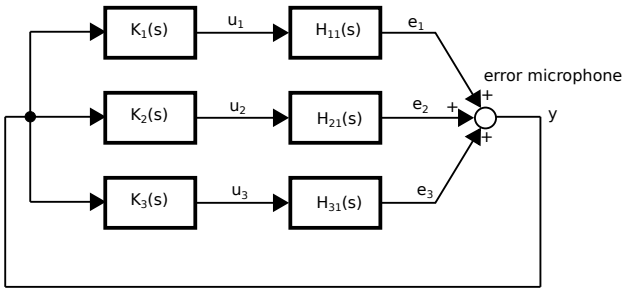


Figure 7: Control problem scheme.

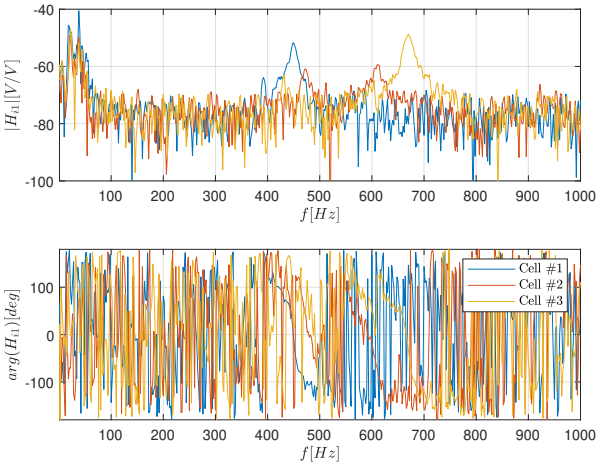


Figure 8: Measured FRF $H_{i1}(f)$ from each cell to error microphone.

Nonetheless, a modal model of the functions $H_{i1}(s)$ is defined using the same methodology and formalism as in [19] assuming the target modes are sufficiently separated in frequency. Hence, the approximation $\hat{H}_{i1}(s)$ is of the form:

$$\hat{H}_{i1}(s) = \sum_{k=1}^{n} \frac{a_k^{i1} + b_k^{i1} s}{s^2 + \omega_k^2 + 2\xi_k \omega_k s} \tag{1}$$

where $k \in [1; n]$ is the target mode number, $\omega_k \in \mathbb{R}^{+*}$ is the mode frequency in rad.s$^{-1}$, $\xi_k \in \mathbb{R}^+$ is the mode damping and $(a_k^{i1}, b_k^{i1}) \in \mathbb{R}^2$ are correction coefficients to obtain the right modal amplitude and

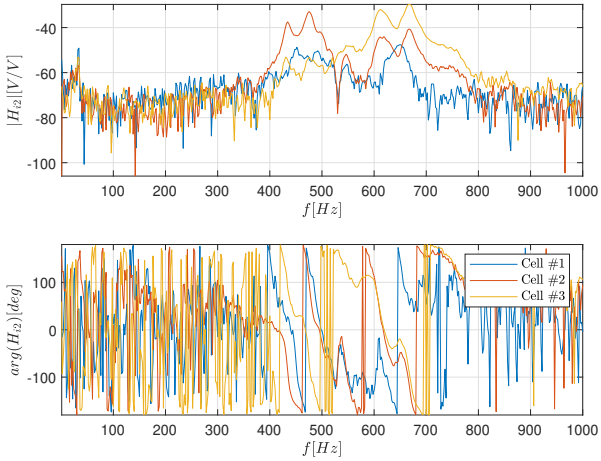


Figure 9: Measured FRF $H_{i2}(f)$ from each cell to laser vibrometer.

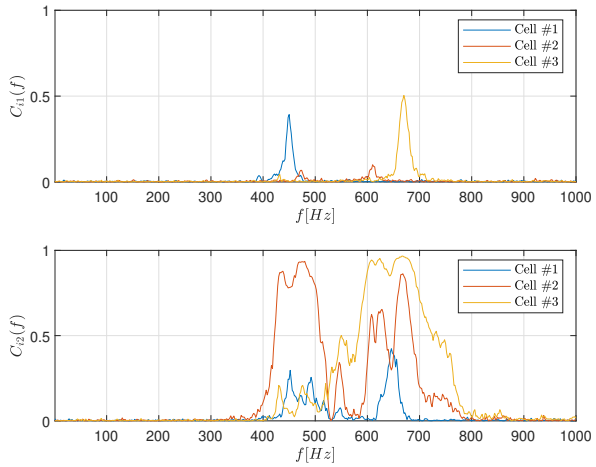


Figure 10: Measured spectral coherences $C_{i1}(f)$ and $C_{i2}(f)$.

phase at $\omega_k$ such that:

$$a_k^{i1} = Re\{H_{i1}(\mathbf{j}\omega_k) \times 2\xi_k \mathbf{j}\omega_k^2\} \quad (2)$$

$$b_k^{i1} = \frac{1}{\omega_k} \times Im\{H_{i1}(\mathbf{j}\omega_k) \times 2\xi_k \mathbf{j}\omega_k^2\} \quad (3)$$

The results of this identification process are summarized in Table 2 and the corresponding estimated functions $\hat{H}_{i1}(f)$ are displayed in Figures 11, 12, and 13. This modal model approximation is especially valid in this context since the controllability of each cell on the error sensor is very narrow in the frequency domain.

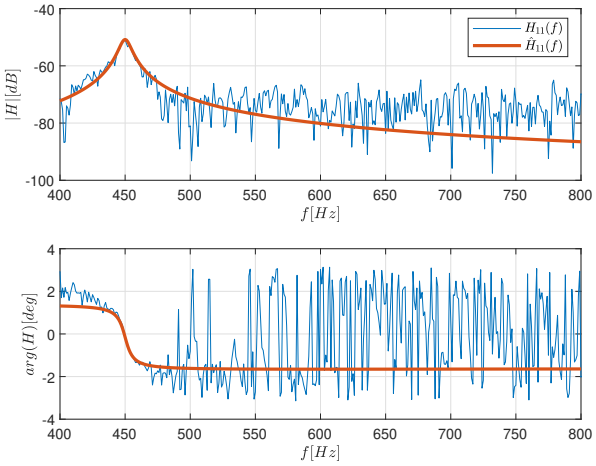


Figure 11: Modal estimation $\hat{H}_{11}(f)$ o measured transfer function $H_{11}(f)$.

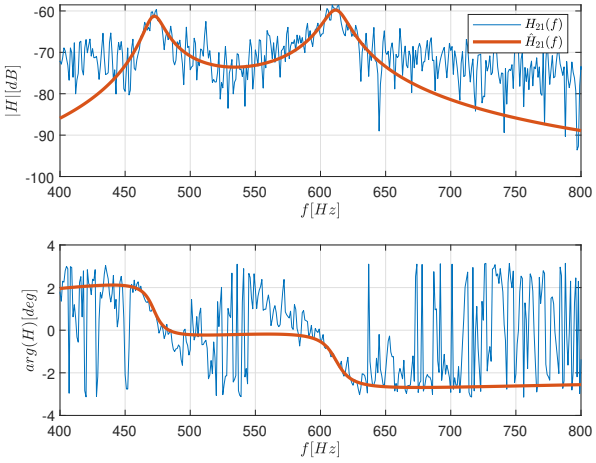


Figure 12: Modal estimation $\hat{H}_{21}(f)$ o measured transfer function $H_{21}(f)$.

### *4.2. Control design*

For control purpose, a state-space realization is then defined for $\hat{H}_{i1}$ as:

$$\hat{H}_{i1} \begin{cases} \dot{x}_i = A_i x_i + B_i u_i \\ e_i = C_i x_i \end{cases} \quad (4)$$

with $A_i \in \mathbb{R}^{2n\times 2n}$, $B_i \in \mathbb{R}^{2n\times 1}$, $C_i \in \mathbb{R}^{1\times 2n}$ and $x_i \in \mathbb{R}^{2n}$ ($D_i = 0$ since $\hat{H}_{i1}$ is strictly proper). The matrices of the aforementioned state-space system are defined by:

$$A_i = \begin{bmatrix} 0_n & I_n \\ -diag(\omega_k^2) & -2diag(\xi_k\omega_k) \end{bmatrix}_{2n,2n} \quad (5)$$

$$B_i = [0_{1,n} \;\; 1_{1,n}]^T \quad (6)$$

$$C_i = [a_1^{i1} \cdots a_n^{i1} \;\; b_1^{i1} \cdots b_n^{i1}] \quad (7)$$

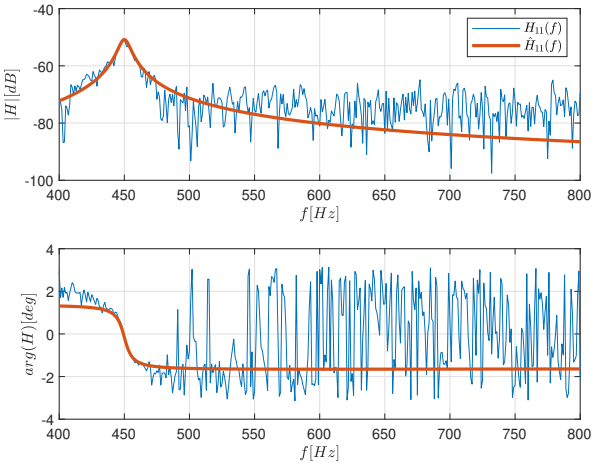


Figure 13: Modal estimation $\hat{H}_{31}(f)$ o measured transfer function $H_{31}(f)$.

| Cell # | $\omega/(2\pi)$ | $\xi$ | $a^{i1}$ | $b^{i1}$ |
|---|---|---|---|---|
| 1 | 450Hz | 0.01 | 71.45 | 0.16 |
| 2 | 472Hz | 0.015 | -186.23 | 0.04 |
| | 612Hz | 0.015 | 440.18 | 0.01 |
| 3 | 670Hz | 0.01 | 724.14 | 0.26 |

Table 2: Identification parameters.

Now that the system is modeled with a state-space representation, the state vector is augmented with a narrow band-pass filter $F_i$ allowing the control from cell #i to focus on the target modes with a tunable bandwidth. Hence, the filter $F_i$ is defined as:

$$F(s) = \frac{1}{1+s^2/\omega_{LP}^2+s/(Q_f\omega_{LP})} \times \frac{s^2/\omega_{HP}^2}{1+s^2/\omega_{HP}^2+s/(Q_f\omega_{HP})} \quad (8)$$

where $Q_f$ is the quality factor and the frequency parameters $(\omega_{HP}, \omega_{LP})$ define the control bandwidth. The system $F_i$ directly filters the measure $y$ and has the following state space representation:

$$F_i \begin{cases} \dot{x}_F &= A_F x_F &+B_F y \\ y_F &= C_F x_F \end{cases} \quad (9)$$

with $A_F \in \mathbb{R}^{m\times m}$, $B_F \in \mathbb{R}^{m\times 1}$, $C_F = I_m$ for the sake of simplicity and $x_F \in \mathbb{R}^m$, $m$ depending on the order of $F_i$. Hence, the augmented system $G_{i1}$ formed by $F_i$ and $\hat{H}_{i1}$ is written as:

$$\begin{bmatrix} \dot{x}_i \\ \dot{x}_F \end{bmatrix} = \begin{bmatrix} A_i & 0 \\ B_F C_i & A_F \end{bmatrix} \begin{bmatrix} x_i \\ x_F \end{bmatrix} + \begin{bmatrix} B_i \\ 0 \end{bmatrix} u_i \quad (10)$$

$$y_F = [0 \;\; C_F] \begin{bmatrix} x_i \\ x_F \end{bmatrix} \quad (11)$$

equivalent to:

$$G_{i1} \begin{cases} \dot{x}_G &= A_G x_G &+B_G u_i \\ y_F &= C_G x_G \end{cases} \quad (12)$$

with

$$x_G = \begin{bmatrix} x_i \\ x_F \end{bmatrix}, A_G = \begin{bmatrix} A_i & 0_{2n\times m} \\ B_F C_i & A_F \end{bmatrix},$$
$$B_G = \begin{bmatrix} B_i \\ 0_{m\times 1} \end{bmatrix}, C_G = [0_{m\times 2n} \;\; C_F] \quad (13)$$

The control gain matrix $M_i \in \mathbb{R}^{1\times(2n+m)}$ such that $u_i = -M_i x_G$ is finally computed for each cell as solution to the LQR problem $(A_G, B_G)$ minimizing the following functional:

$$J = \frac{1}{2}\int_{-\infty}^{+\infty} x_G^T Q x_G + u_i^T R u_i \quad (14)$$

with $Q = diag\left([0_{1,2n} \;\; 1_m]\right) \times 10^2$ to control essentially within the bandwidth driven by $F_i$ and $R = 10^{-4}$. Since only partial feedback is available from the filter output $y_F$, a Kalman filter is designed to estimate the full state $x_G$ and the total controller is written as:

$$\dot{\hat{x}}_G = A_G \hat{x}_G + B_G u_i + L\left(y_G - C_G \hat{x}_G\right) \quad (15)$$
$$u_i = -M_i \hat{x}_G \quad (16)$$

where $\hat{x}_G$ is the state estimation. The observer gain matrix $L \in \mathbb{R}^{(2n+m)\times m}$ is computed considering a high level covariance in the state perturbation, allowing faster convergence to the real state. A scheme of the final controller $K_i$ architecture is displayed on Figure 14.

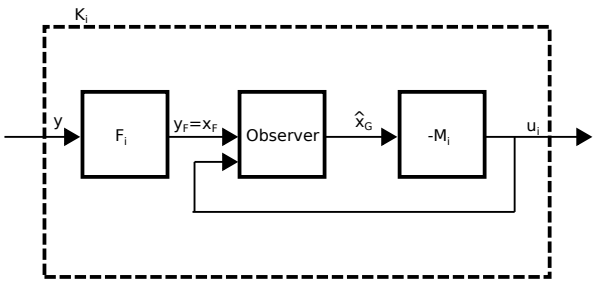


Figure 14: Controller $K_i$ architecture.

## 5. Experimental results

This final section presents the results obtained in terms of active acoustic control in the experimental setup considered for airflow velocities up to 20m.s$^{-1}$ in the wind tunnel. As primary acoustic perturbation, a band-limited white noise is applied to a loudspeaker amplifier at a sampling frequency of 50kHz (see Figure 5) with the actuator positioned upstream with respect to the active device. For each airflow velocity, the active noise control system is then switched on to observe its performance.

The Figures 15 and 16 display first the power spectral density (PSD) of the voltage signals coming from the downstream microphone #3 and upstream microphone #2 respectively, for all the experimental cases of control and airflow. One can immediately notice the low-frequency impact (see zoom section under 100Hz) of the airflow within the duct. This observation is very positive since the control must operate at higher frequencies. Hence, the airflow should not interfere with the three control closed loops. The zoom section around the narrow bandwidth impacted by the control (620-712Hz) confirms the previous conclusion since the control effect on the PSD of both downstream and upstream microphones is indeed not affected by the flow velocity. In terms of performance, a maximum attenuation of 4 dB is achieved on microphone #3, and only around 670Hz demonstrating that the cells #1 and #2 are almost inefficient compared to cell #3. As mentioned earlier, there is still a lot of dispersion in the manufacturing process of the proposed prototypes, creating discrepancies in the electro-mechanical behavior. Besides, the acoustic level within the controlled bandwidth is increased upstream by the same attenuation factor at the downstream positions. Nevertheless, this level of attenuation is still interesting as it mainly demonstrates the physical and technological ability of the system to interact with grazing incidence acoustic waves and impact the global downstream acoustic field.

Figure 17 summarizes these results by computing a ratio between the PSD of the downstream microphone signal with and without control with the mentioned reduction of 4dB at 670Hz.

Figures 18 and 19 show approximations of the transmission loss (TL) and insertion loss (IL). The TL represents the ratio between the incident sound power on the sample and the sound power transmitted by the sample :

$$TL = 10log_{10}\left(\left|\frac{A}{C}\right|^2\right) \tag{17}$$

where $A$ and $C$ are the complex coefficients of the transmission matrix [20] corresponding to the incident waves. Then, the IL represents the difference between the TL of the reference rigid liner and the TL from the considered control system.

$$IL = TL - TL_{ref} \tag{18}$$

Hence, a 2.5dB gain is achieved by the proposed piezoelectric active control system around the main controlled frequency of 670Hz on the IL, providing good confidence in this technological solution to control future acoustic sources coming from the interaction between turbulence and airfoil. Finally, the RMS values of the voltage control signal of each cell, for every airflow velocity are displayed in Figure 20. As observed previously, the actual airflow had no impact on the control bandwidth and the necessary control energy is not affected. A time domain extract of the control signal $u_1(t)$ with the extreme cases of airflow velocity is also plotted to illustrate this phenomenon.

### *5.1. Comparison with a passive solution*

A passive solution to reduce the noise emission due to the interaction between a turbulent flow and airfoil is being developed within the same project. Its design relies on the previous work from Bampanis et al. [21]. Hence, samples had been tested in a similar wind tunnel, using the same sample holder dimensions as the one presented in Figure 4. These experiments also took interest in the absorption of acoustic waves with a grazing incidence in presence of airflow.

The measured IL for one of the samples is now compared to the active solution without airflow in Figure 21. These results show that the passive solution achieves a moderate broadband performance on the IL while the active solution presents a higher level of IL, but over a very narrow frequency band corresponding to the identified controlled electromechanical mode. This observation confirms that a future better-designed actuator with higher piezoacoustic coupling and larger bandwidth could offer better performance than passive solutions and use less space than hybrid systems with resonators.

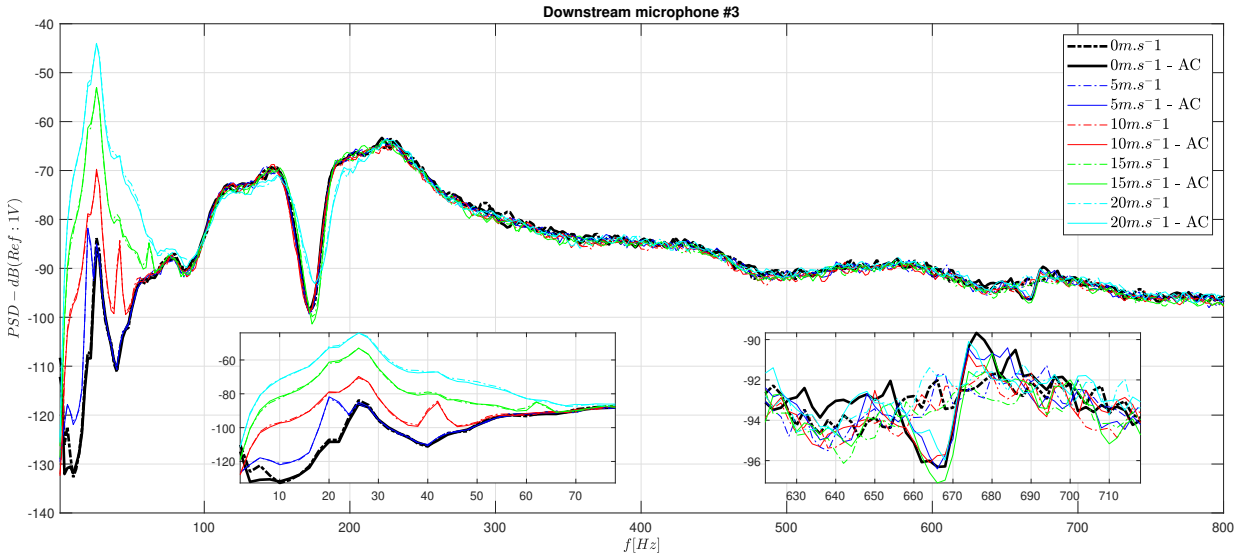


Figure 15: Downstream microphone #3 signal PSD for all values of airflow velocity, AC: Active Control.

## 6. Conclusion and perspectives

This manuscript presented experimental results on the early development of a newly designed active acoustic control system dedicated to stator vanes for jet engines consisting of flush-mounted piezoelectric cells. The idea behind this technological implementation was to control the noise created by turbulence interacting with the airfoil profile and also not disturb the airflow to maintain aerodynamic performance. Three active cells have been placed into a wind tunnel with a primary acoustic source and an anechoic termination. Based on a modal identification of the piezoacoustic behavior of each cell, a linear MSISO controller has been designed to provide narrow-band rejection performance to the system due to its resonant characteristics. Thus, attenuation of 4dB around the main controlled mode at 670Hz has been achieved on the target downstream microphone PSD, increasing also the acoustic level on the upstream microphone as a side effect. A corresponding insertion loss of 2.5dB has been reached for the considered bandwidth. The most interesting result is certainly that such performance level has been achieved with all values of experimented airflow velocities up to 20m.s$^{-1}$. Since the proposed active control system is currently in an early prototyping phase, the actual results are modest. Nevertheless, they provide good confidence for a future better-designed actuator with higher piezoacoustic coupling to be able to control acoustic disturbances coming from real turbulence interacting with the vane leading edge.

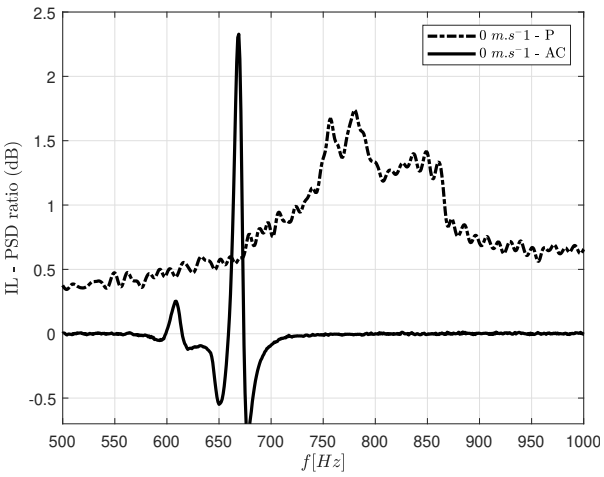


Figure 21: Comparison of the insertion loss IL in [dB] between the active and the passive materials without flow. P: passive material made of melamine foam covered with wire mesh.

## 7. Declarations

### *7.1. Funding*

This project has received funding from the Clean Sky 2 Joint Undertaking (JU) under agreement n°865007. The JU receives support from the European Union's Horizon 2020 research and innovation

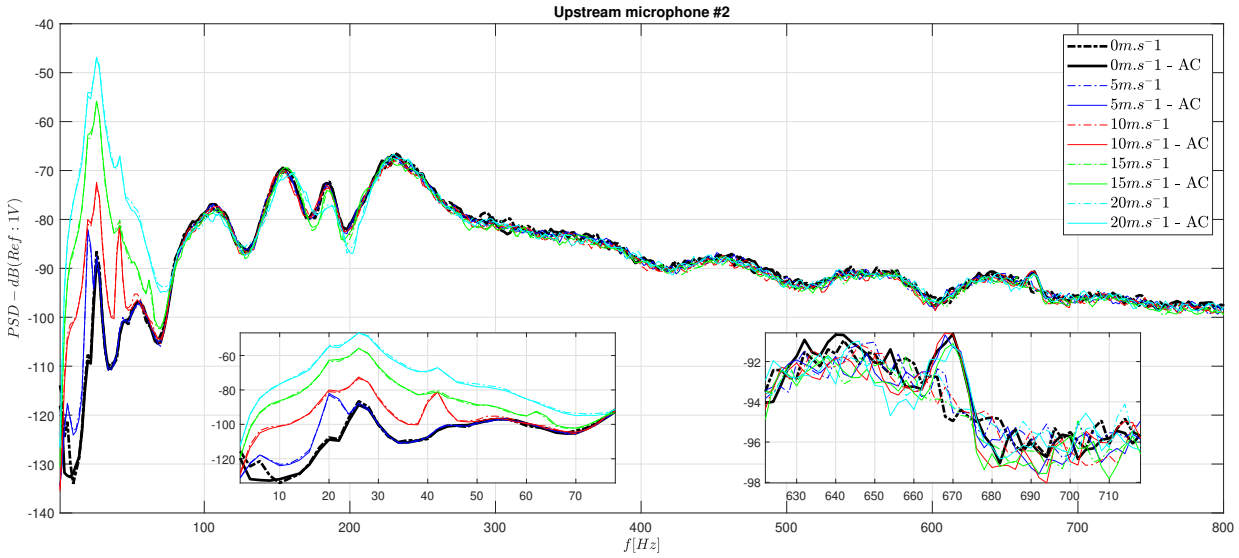


Figure 16: Upstream microphone #2 signal PSD for all values of airflow velocity, AC: Active Control.

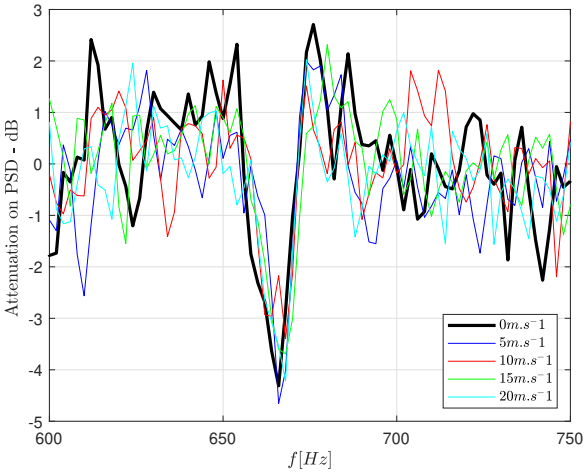


Figure 17: Active control effect in [dB] on downstream microphone #3 signal PSD for all values of airflow velocity.

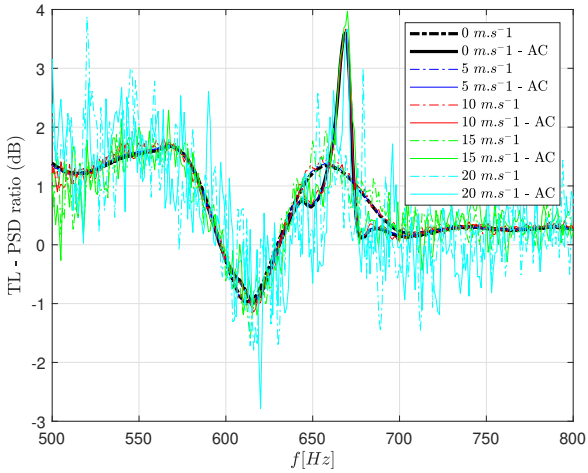


Figure 18: Transmission loss approximation in [dB] between the downstream microphones (#3 and #4) and the upstream microphones (#1 and #2) for all values of airflow velocity.

program and the Clean Sky 2 JU members other than the Union. This publication reflects only the author's view and the JU is not responsible for any use that may be of the information it contains.

### *7.2. Conflicts of interest*

The authors declare no conflict of interest.

## References

[1] Desquesnes, G., Terracol, M., & Sagaut, P. (2007). *Numerical investigation of the tone noise mechanism over laminar airfoils.* Journal of Fluid Mechanics, 591, 155-182.

[2] Envia, E. (2002). Fan noise reduction: an overview. International Journal of Aeroacoustics, 1(1), 43-64.

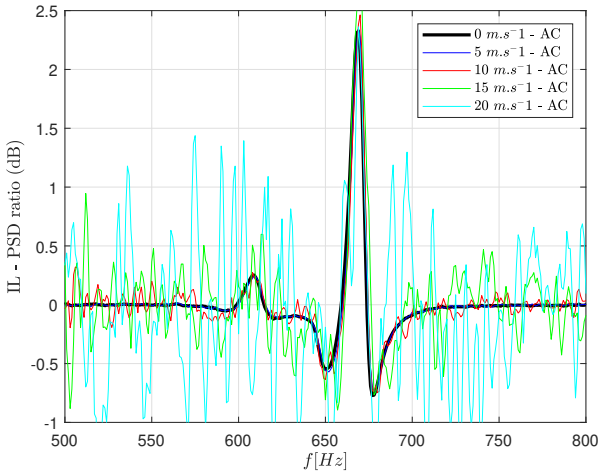


Figure 19: Insertion loss approximation in [dB] between the downstream microphones (#3 and #4) and the upstream microphones (#1 and #2) for all values of airflow velocity.

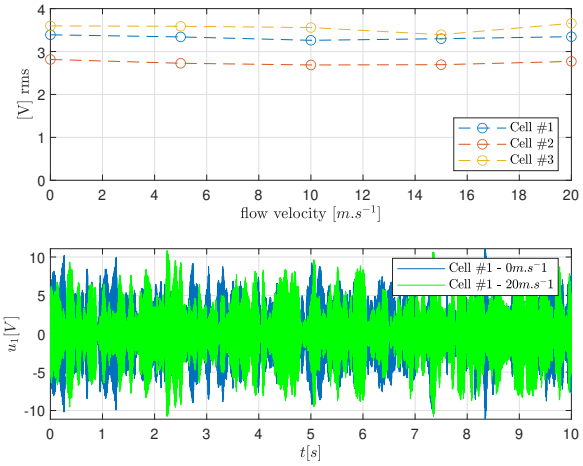


Figure 20: Control signal RMS value for each cell and all values of airflow velocity, $u_1(t)$ with no airflow and maximum velocity airflow.


[3] Neise, W., & Enghardt, L. (2003). *Technology approach to aero engine noise reduction*. Aerospace Science and Technology, 7(5), 352-363.

[4] Huff, D. L. (2007, September). *Noise reduction technologies for turbofan engines*. In 35th International Congress and Exposition on Noise Control Engineering (INTER-NOISE 2006) (No. E-15787).

[5] Liu, X., Zhao, D., Guan, D., Becker, S., Sun, D., & Sun, X. (2022). *Development and progress in aeroacoustic noise reduction on turbofan aeroengines*. Progress in Aerospace Sciences, 130, 100796.

[6] Envia, E., Huff, D., & Morrison, C. (1996). *Analytical assessment of stator sweep and lean in reducing rotor-stator tone noise*. In Aeroacoustics Conference (p. 1791).

[7] Hansen, K., Kelso, R., & Doolan, C. (2012). *magenta*Reduction of flow induced airfoil tonal noise using leading edge sinusoidal modifications. Acoustics Australia, 40(3), 172-177.

[8] Vemuri, S. S., Liu, X., Zang, B., & Azarpeyvand, M. (2020). *On the use of leading-edge serrations for noise control in a tandem airfoil configuration*. Physics of Fluids, 32(7), 077102.

[9] Eldredge, J. D., & Dowling, A. P. (2003). *The absorption of axial acoustic waves by a perforated liner with bias flow*. Journal of Fluid Mechanics, 485, 307-335.

[10] Geyer, T., Sarradj, E., & Fritzsche, C. (2010). *Measurement of the noise generation at the trailing edge of porous airfoils*. Experiments in fluids, 48(2), 291-308.

[11] Vinogradov, I., & Zhou, Y. (2014). *Stator Vane-Based Active Control of Turbofan Engine Noise*. In Fluid-Structure-Sound Interactions and Control (pp. 247-252). Springer, Berlin, Heidelberg.

[12] Carneal, J. P., Giovanardi, M., Fuller, C. R., & Palumbo, D. (2008). *Re-Active Passive devices for control of noise transmission through a panel*. Journal of Sound and Vibration, 309(3-5), 495-506.

[13] Ripamonti, F., Giampà, A., Giona, R., Liu, L., & Corradi, R. (2022). *Numerical and experimental study of an active control logic for modifying the acoustic performance of single-layer panels*. Journal of Sound and Vibration, 520, 116608.

[14] Carmona, J. C., & Alvarado, V. M. (2000). *Active noise control of a duct using robust control theory*. IEEE Transactions on control systems technology, 8(6), 930-938.

[15] Curtis, A. R. (1999). *Active control of fan noise by vane actuators* (No. E-11704).

[16] Galland, M. A., Mazeaud, B., & Sellen, N. (2005). *Hybrid passive/active absorbers for flow ducts. Applied acoustics*, 66(6), 691-708.

[17] Sellen, N., Cuesta, M., & Galland, M. A. (2006). *Noise reduction in a flow duct: Implementation of a hybrid passive/active solution*. Journal of sound and vibration, 297(3-5), 492-511.

[18] Perez, M., Ezzine, M., Billon, K., Clair, V., Mardjono, J. and Collet, M., 2020, September. *Design and Optimization of Piezoelectric Actuators for Aeroacoustic Noises Control in a Turbofan*. In Smart Materials, Adaptive Structures and Intelligent Systems (Vol. 84027, p. V001T02A010). American Society of Mechanical Engineers.

[19] Rodriguez, J., Collet, M., & Chesné, S. (2021). *Experimental modal identification of smart composite structure applied to active vibration control*. Smart Materials and Structures, 30(11), 115008.

[20] Ingard, K. U., & Dear, T. A. (1985). *Measurement of acoustic flow resistance*. Journal of Sound Vibration, 103(4), 567-572.

[21] Bampanis, G., Roger, M., & Moreau, S. (2022). *On a three-dimensional investigation of airfoil turbulence-impingement noise and its reduction by leading-edge tubercles*. Journal of Sound and Vibration, 520, 116635.